J Mater Sci: Mater Electron **(2025) 36:764**

Optical and structural properties of ZnO/TiO_2 bilayer thin films deposited by pulsed DC magnetron sputtering

Mohammed H. Fawey[1,*], A. A. Abd El-Moula[1,2], F. M. El-Hossary[1], Tawheed Hashem[3,4], and M. Abo El-Kassem[1]

[1] *Physics Department, Faculty of Science, Sohag University, Sohag 82524, Egypt*
[2] *Physics Department, College of Science, Jouf University, 2014 Sakaka, Jouf, Saudi Arabia*
[3] *Karlsruhe Institute of Technology (KIT), Institute of Functional Interfaces (IFG), KIT-Innovation HUB, Hermann-von-Helmholtz Platz-1, 76344 Eggenstein-Leopoldshafen, Germany*
[4] *Center for Materials Science, Zewail City of Science and Technology, 6th of October, Giza 12578, Egypt*

Received: 19 February 2025
Accepted: 29 March 2025
Published online: 29 April 2025

ABSTRACT

Pulsed DC magnetron sputtering was employed to deposit ZnO/TiO_2 bilayer thin films of varying thicknesses on glass substrates, with both layers being 80 nm thick. The structural and optical properties of the thin films were investigated using X-ray diffraction (XRD), atomic force microscopy (AFM), photoluminescence (PL), and optical transmittance measurements. The AFM analysis revealed a fine dispersion of spherical particles on the bilayer, with thicker ZnO layers leading to an increase in particle size. The single-layer film exhibited lower surface roughness (4.56 nm and 4.71 nm for ZnO and TiO_2, respectively) compared to the ZnO/TiO_2 bilayer (approximately 8 nm). The adhesion force decreased with increasing TiO_2 thickness, from 50 mN (80 nm ZnO) to 10 mN (80 nm TiO_2). XRD analysis indicated that the ZnO/TiO_2 bilayer are amorphous, while the single ZnO layer is semi-crystalline with a hexagonal wurtzite crystal structure with an average crystallite size of 52 nm for the ZnO (100) plane. PL spectroscopy showed a strong violet emission at 420 nm, along with weaker emissions at 461 and 467 nm for all samples. The intensity of UV emission increased with TiO_2 layer thickness, peaking at 20 nm ZnO/60 nm TiO_2. The band gaps (E_g) for the single-layer ZnO and TiO_2 were found to be 3.21 eV and 3.32 eV, respectively. However, the E_g of the bilayer films increased from 3.27 eV to 3.36 eV as the TiO_2 layer thickness increased.

Address correspondence to E-mail: mohammed.fawey@gmail.com

https://doi.org/10.1007/s10854-025-14703-4

1 Introduction

Zinc oxide is a common II–VI compound semiconductor with a large direct band gap (3.2–3.4 eV), low cost, and non-toxicity [1, 2]. It exhibits strong optical transmission and is well suited for the solar spectrum [1]. Due to its structural, electrical, and optical properties, ZnO has a wide range of applications in optoelectronic devices and solar cells [3–6]. Owing to these promising characteristics, ZnO thin films have attracted significant attention in the literature [1, 7–9]. On the other hand, titanium dioxide (TiO_2) is an important semiconductor with numerous applications in photocatalysis and optoelectronic devices [10–12]. In addition, with the advent of 5G technology in mobile communication systems, there is an increasing demand for miniature, high-frequency microwave devices, where dielectric materials, including magnetodielectrics, are highly sought after [13–15]. For example, D. A. Vinnik et al. demonstrated that titanium-substituted barium hexaferrites exhibit tailored magnetodielectric behavior, which is essential for microwave applications [15]. Furthermore, various classes of oxides have shown excellent electronic properties [16]. The microstructural, optical, and electrical properties of TiO_2 thin films are influenced by the deposition techniques and the types of TiO_2 phases that are formed [17–20].

On the other hand, multilayered semiconductor materials can be able to improve the electrical and optical properties of films [21–23]. It is well known that combining different compounds with excellent dielectric properties leads to the formation of new composite materials, which have garnered significant technological interest in recent years [24]. Furthermore, the combination of polymers with oxides results in composites with enhanced electronic properties [25]. In recent years, the combination of ZnO and TiO_2 in bilayer thin films has gained significant attention as a promising strategy to harness the complementary properties of both semiconductors. This approach has shown enhanced performance in applications such as photovoltaics, photocatalysis, and optoelectronics [26–29]. Recent studies on zinc-titanium-based compounds have highlighted their unique properties. For example, Barros et al. examined the high thermal stability of $ZnNb_2O_6$ with $CaTiO_3$ addition, showing its potential for microwave dielectric applications in the C- and S-bands [30]. In addition, Bodnar et al. produced single crystals of $Cu_2ZnGeSe_4$ using a gas chemical method and observed a 12% increase in the band gap as the temperature decreased from 300 to 20 K [31]. The bilayer architecture provides distinct advantages, including improved charge separation, extended optical absorption, and an increased surface area for catalytic processes. Specifically, the use of TiO_2 as a bottom layer enhances stability and photocatalytic efficiency, while the ZnO top layer contributes to superior optical and electronic properties. Together, these layers create a synergistic effect, achieving performance metrics unattainable by either material alone. For use in solar cells and light-emitting diodes, optimized multilayered ZnO films can be created with low resistivity and high solar transparency in the visible spectrum [32].

Various techniques are employed to fabricate thin films, including atomic layer deposition (ALD) [33], chemical vapor deposition (CVD) [34], DC magnetron sputtering [35, 36], spray pyrolysis [37], and sol–gel [38]. Moreover, there are other methods for the synthesis of oxide particles such as standard solid-state reaction [39] and ion-beam sputtering/deposition (IBSD) technique [40]. Among these, DC magnetron sputtering stands out due to its numerous advantages, such as low synthesis temperature, cost-effectiveness, precise control over film thickness and composition, and the ability to produce homogeneous thin-film microstructures. In addition, this technique is highly promising for its capacity to deposit thin, transparent, and uniform layers on diverse substrates with high efficiency and low cost. As a result, DC magnetron sputtering is widely utilized for depositing materials with a range of properties [41–46], including metal oxide thin films [47–49]. In particular, DC magnetron sputtering enables the fabrication of ZnO and TiO_2 thin films with tailored properties by adjusting sputtering parameters, such as power, pressure, and deposition time [50, 51].

The structure and properties of photocatalytic films produced via magnetron sputtering are influenced by various factors, including the working pressure, O_2/Ar ratio, the distance between the substrate and target, the type and temperature of the substrate, the sputtering power, and the configuration of the target [52, 53].

For example, oxygen stoichiometry plays a crucial role in determining the electrical and structural properties of complex oxides [25]. One of the most important parameters influencing the optical properties of deposited thin films is their thickness. The thickness of TiO_2 and ZnO layers plays a critical role in shaping their optical characteristics. By carefully adjusting the thickness, it becomes possible to optimize these properties for specific applications, such

as high-transmittance coatings, UV protection, or enhanced light absorption in solar cells. Both experimental and theoretical studies often focus on fine-tuning the thickness to achieve an optimal balance between transmittance, reflectance, and absorbance [54, 55]. For instance, C.M. Firdaus et al. [56] explored the performance and characteristics of nanostructured ZnO and ZnO/TiO_2 thin films on glass substrates, fabricated using the sol–gel spray-spin coating technique at varying thicknesses. Their study revealed that the conductivity of the ZnO/TiO_2 nanocomposite was higher compared to that of the pure ZnO nanostructures. Furthermore, optical properties demonstrated that the band gap of the ZnO/TiO_2 nanocomposite decreased with increasing thickness. I. Saurdi et al. [57] investigated the effect of TiO_2 thickness on ZnO nanorod/ TiO_2 nanocomposites. TiO_2 films were deposited on glass substrates at various thicknesses using the spin coating method. Their results showed that the solar energy conversion efficiency (η) of 2.543% under AM1.5 was achieved for the ZnO nanorod/TiO_2 dye-sensitized solar cells with a TiO_2 thickness of 2710 µm, showing higher dye desorption and absorbance compared to other configurations. However, there is limited research on the effects of combining these materials in bilayer configurations, particularly with DC-pulsed magnetron sputtering. As a result, the relationship between layer thickness, structural morphology, and optical properties remains poorly understood.

This study offers new insights into the relationship between layer thickness and the properties of ZnO/TiO_2 bilayer films, specifically exploring how variations in the individual layer thicknesses influence surface roughness, adhesion force, structural integrity, and optical characteristics. By maintaining a constant total bilayer thickness of 80 nm while altering the thickness of the ZnO and TiO_2 layers, this research uniquely investigates the effects of thickness ratio on the films' performance for optoelectronic applications. The novelty of this work lies in its systematic examination of how these structural and optical properties can be tailored through controlled adjustments in layer thickness, providing valuable guidance for optimizing bilayer films for future photocatalytic and optoelectronic technologies.

2 Experimental details

The current study involves the deposition of titanium dioxide (TiO_2) and zinc oxide (ZnO) thin films onto glass substrates using pulsed DC magnetron sputtering technology. A schematic representation of the system can be found in a previous publication [58]. The deposition chamber is equipped with three guns, each capable of depositing thin films, duplex layers, multilayers for specific applications, or multifunctional coatings. By operating two or three guns simultaneously, alloy thin films can be grown from different targets. The thickness monitor (Inficon SQM-160), integrated into the sputtering chamber, was used to monitor both the deposition rate and the thickness of the multilayer film. In addition, the target-to-substrate distance can be adjusted within a range of 7 cm to 20 cm. The sample holder, and consequently the substrates, can be heated to temperatures of up to 900 °C. These parameters can be varied and optimized during the preparation of the thin films. In this study, a 1-mm-thick glass sheet was cut into coupons measuring 20 mm × 10 mm. Before being introduced into the deposition chamber, the glass substrates were ultrasonically cleaned in methanol for 15 min. The anode, which functions as the sample holder, has a diameter of 50.8 mm and is designed to hold the substrates in front of the three guns. The anode has the advantage of rotating from 0° to 360° and vice versa during deposition, ensuring a homogeneous and uniform film. The rotation speed is controlled using a Programmable Oscillation Controller (model no: DCS-GP-SMC-2K12). Each of the three guns can be equipped with a different target, also 50.8 mm in diameter, eliminating the need to evacuate the chamber and replace the target after depositing each layer. The targets are cooled during the deposition process using an industrial chiller (model: CW-5200), with the cooling water temperature set to 10 °C.

For this work, a titanium (Ti) target with a thickness of 3 mm and 99.99% purity was used in a mixture of argon (Ar) and oxygen (O_2) gases to deposit a TiO_2 coating on the glass substrates. Subsequently, a different Ar/O_2 gas ratio was employed to deposit a thin ZnO layer using a Zn target of 3 mm thickness and 99.99% purity. Once the substrates were placed in the chamber, the target-to-substrate distance was precisely set to 7 cm. Next, a two-stage rotary pump and a turbomolecular pump were used to evacuate the chamber, reducing the pressure to 7×10^{-6} mbar over 1.5 h.

Following this, O_2 as the reactive gas and Ar were introduced into the chamber, raising the gas pressure from 7×10^{-6} mbar to approximately 5×10^{-3} mbar. For the deposition of ZnO thin films, a gas mixture consisting of 10% O_2 and 90% Ar was used. For the deposition of TiO_2 thin films, a gas mixture of 5% O_2 and 95% Ar was employed. The anode rotation speed was set to complete a full 360° cycle every 15 s, alternating between clockwise and counterclockwise rotations. Once the gases were introduced and the working pressure was stabilized, a pulsed DC generator (AE Advanced Energy Pinnacle Plus) was used to power the Ti or Zn target, initiating the deposition process. The pulsed DC generator was configured with a pause duration of 2 μs and a frequency of 150 kHz. The input power was set to 50 W for ZnO deposition and 150 W for TiO_2 deposition. All samples were prepared under identical conditions, with the only variable being the thickness of the deposited layer. The initial thickness of the first layer (TiO_2) was set to 10 nm and was incrementally increased by 10 nm until reaching a final thickness of 70 nm. Conversely, the initial thickness of the second layer (ZnO) was 70 nm and was incrementally decreased by 10 nm to achieve a final thickness of 10 nm. The total combined thickness of the two deposited layers was 80 nm. It is worth noting that, prior to initiating the bilayer deposition, the deposition rates for ZnO and TiO_2 were measured under the same conditions used during the deposition process. The measured deposition rate for ZnO was 1.57 Å/s, while for TiO_2, it was 0.23 Å/s. After completing the deposition process, the samples were allowed to cool for 15 min before the chamber was vented to atmospheric pressure.

The multilayers were characterized analytically post-deposition. XRD measurements were conducted to analyze the structural properties of the thin films using a Bruker D8 ADVANCED diffractometer. The instrument was equipped with Cu Kα radiation ($\lambda = 1.5406$ Å) and operated at a scanning speed of 2° min^{-1} with a step size of 0.02°. The 2θ scanning range was set from 10° to 90°, allowing for a comprehensive analysis of the crystalline phases and structural characteristics of the thin films. This setup enabled the identification of lattice parameters, crystallite size, and phase composition, providing detailed insights into the structural properties of the samples. Moreover, AFM measurements were performed to evaluate the surface smoothness of the monolayer and bilayer films at the nanometer scale. AFM measurements were conducted using a Bruker Icon atomic force microscope (Germany) operating in tapping mode, with NSC15/Al-BS cantilevers at a scan rate of 0.295 Hz. In addition, optical transmittance measurements were conducted to characterize the thin films' optical properties (absorbance, transmittance, and band gap) using a double-beam UV–visible spectrophotometer (Jasco V-760, USA), covering a wavelength range of 300 to 2000 nm. Furthermore, the PL measurements were performed using a Jasco FP-6500 spectrofluorometer (Japan), equipped with a 150 Watt Xenon arc lamp as the excitation source. The slit bandwidth for both the excitation and emission monochromators was fixed at 5 nm, ensuring precise wavelength control and minimizing spectral overlap. All measurements were performed at room temperature (RT) under consistent geometrical conditions to ensure reproducibility and accuracy.

3 Results and discussion

3.1 Morphological properties

Figure 1 presents AFM images of single-layer and bilayer ZnO/TiO_2 films with the same overall thickness. Figure 1 shows a uniform distribution of spherical particles on both the single-layer ZnO and TiO_2 films. In contrast, the bilayer exhibits small spherical particles on the surface, with particle size increasing as the thickness of the top ZnO layer increases. Table 1 provides the measured surface roughness (Ra in nm) and adhesion force (in mN) derived from the topographic images. The results show that the surface roughness of the single-layer ZnO and TiO_2 films is lower compared to that of the ZnO/TiO_2 bilayer. The surface roughness was measured to be 4.56 nm for the ZnO single layer and 4.71 nm for the TiO_2 single layer, while the surface roughness of the ZnO/TiO_2 bilayer was approximately 8 nm. The roughness at the interface between the two layers may contribute to the increased surface roughness of the bilayer, influencing the overall surface profile. In addition, stress at the interface, arising from mismatches between adjacent layers, may further contribute to the increase in surface roughness [59]. Furthermore, adhesion force measurements revealed that the critical load required to peel the ZnO thin film from the substrate was 50 mN, while for TiO_2, it was only 10 mN. As summarized in Table 1, the adhesion force for the bilayer

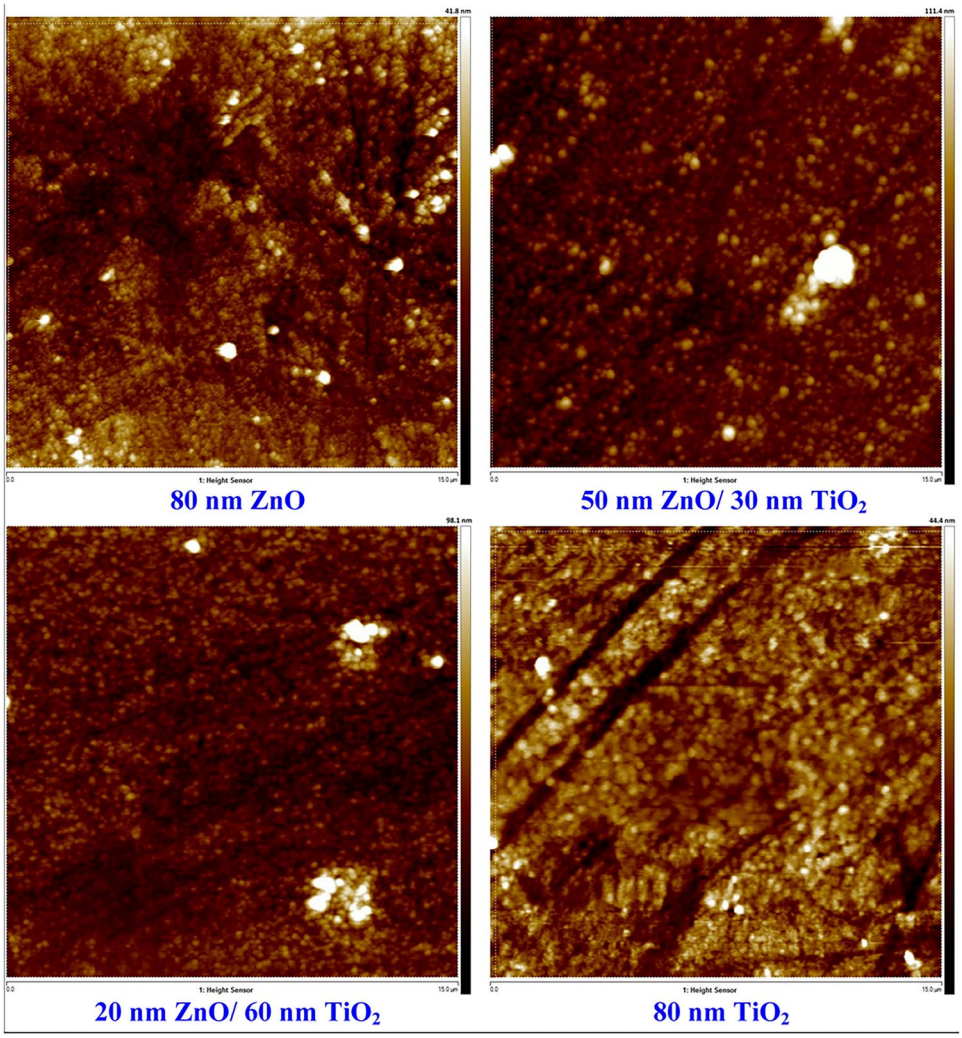

Fig. 1. 2D AFM topography images ($15 \times 15\ \mu m^2$) of 80 nm TiO_2, 80 nm ZnO, 20 nm ZnO/60 nm TiO_2, and 50 nm ZnO/30 nm TiO_2 thin films

Table 1 Band-gap energy (E_g), surface roughness (Ra), and adhesion force (mN) of ZnO/TiO_2 thin films

Samples	E_g (eV)	Ra (nm)	Adhesion force (mN)
80 nm ZnO	3.21	4.56	50
50 nm ZnO/30 nm TiO_2	3.27	8.46	35
20 nm ZnO/60 nm TiO_2	3.36	8.12	25
80 nm TiO_2	3.32	4.71	10

increased with ZnO thickness, ranging from 25 mN for a 20 nm ZnO/60 nm TiO_2 bilayer to 35 mN for a 50 nm ZnO/30 nm TiO_2 bilayer. The higher adhesion force for ZnO compared to TiO_2 can be attributed to ZnO's higher surface energy and lower stiffness, which enhance its adhesion to the bottom layer and substrate [60]. In addition, the wurtzite structure of ZnO may provide a better lattice match with the substrate, contributing to stronger adhesion.

3.2 Structural properties

The XRD patterns of single-layer and bilayer ZnO/TiO_2 films deposited on a glass substrate are shown in Fig. 2, with a total film thickness of approximately 80 nm. The results reveal that the single ZnO layer is semi-crystalline, exhibiting a diffraction peak at 31.67° corresponding to the (100) plane of ZnO, and a very weak diffraction peak at 33.8° for the (002) plane. According to the standard JCPDS card (36–1451), these peaks confirm the hexagonal wurtzite crystal structure, with the c-axis oriented parallel to the substrate surface. The average crystallite size for the ZnO (100) plane is approximately 52 nm, calculated using the Scherrer equation [61]:

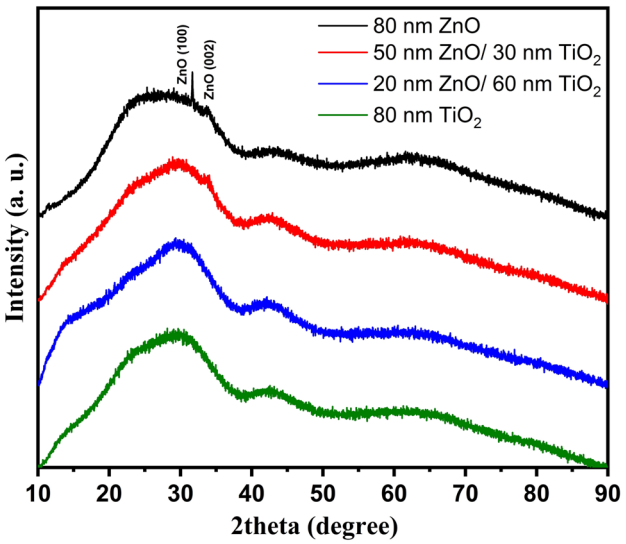

Fig. 2 XRD patterns of single-layer ZnO, single-layer TiO_2, and bilayer ZnO/TiO_2 thin films

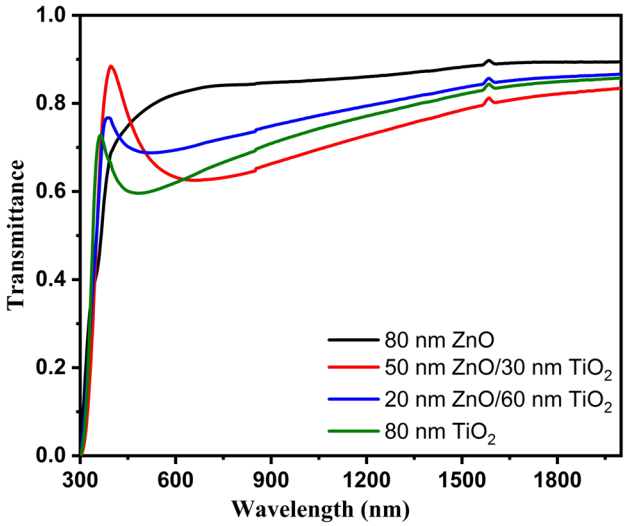

Fig. 3 Transmittance spectra of single-layer ZnO, single-layer TiO_2, and bilayer ZnO/TiO_2 thin films

$$D = \frac{K\lambda}{\beta\cos\theta}, \quad (1)$$

where D is the average crystallite size, K is the Scherrer constant (approximately 0.9), λ is the X-ray wavelength, β is the full-width at half-maximum (FWHM), and θ is the diffraction angle (Bragg angle).

The XRD pattern of the single TiO_2 layer exhibits an amorphous structure (Fig. 2), consistent with the findings of Sagidolda et al. [62], who reported an amorphous structure for TiO_2 thin films deposited by RF magnetron sputtering with a thickness of approximately 125 nm. In contrast, the ZnO/TiO_2 bilayer films show an amorphous structure when the top ZnO layer is thin (20 nm), with a very weak diffraction peak at 33.8° for the (002) ZnO plane that becomes more prominent as the top ZnO layer thickness increases to 50 nm. The amorphous nature of the bilayer ZnO/TiO_2 films is likely attributed to the thinness of the ZnO top layer and the stress at the interface between the bilayers. In addition, the amorphous TiO_2 bottom layer may hinder the crystal growth of ZnO [63].

3.3 Optical properties

Figure 3 illustrates the transmittance spectra of four samples: TiO_2 single layer, ZnO single layer, 20 nm ZnO/60 nm TiO_2, and 50 nm ZnO/30 nm TiO_2. The sharp decline in transmission in the UV region can be explained by the optical band gap. Figure 3 also shows a clear redshift in the absorption edge with increasing ZnO thickness, which aligns with the band-gap values as summarized in Table 1. Notably, the transparency of the 80 nm ZnO film is greater than that of the 80 nm TiO_2 film. This difference can be attributed to the semi-crystalline structure of ZnO, in contrast to the amorphous structure of TiO_2, which may enhance light scattering and absorption, thereby reducing transmittance. The AFM images also reveal that the bilayer has a rougher surface compared to the single layers of ZnO and TiO_2, which may contribute to the reduced light transmission. This reduction in transmittance could be attributed to light scattering caused by the rough surface morphology and the amorphous structure of the bilayer films. When compared to the single-layer ZnO film, the bilayer exhibits lower transmittance. Previous studies have shown that thin films with smoother surfaces and fewer grain boundaries tend to have higher transmittance in the visible range [64, 65]. Y. Chen et al. [66] observed that as the ZnO layer on TiO_2 increased in thickness, the transmittance spectra decreased in the 500–800 nm range, followed by an increase in transmittance from 400 to 500 nm. These findings are consistent with the present data. It is likely that the rougher surface and higher grain boundary density of the films lead to increased optical scattering, which reduces the transmittance around 500 nm [66]. Moreover, Fig. 4 shows the variation of the absorption coefficient across the wavelength range of 300 to

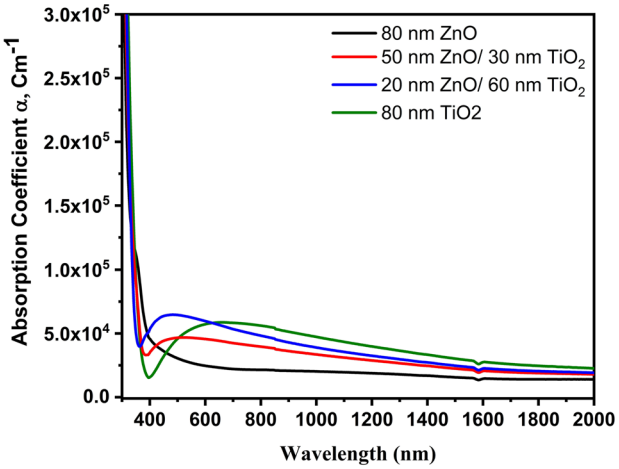

Fig. 4 Absorption coefficient of single-layer ZnO, single-layer TiO_2, and bilayer ZnO/TiO_2 thin films across a range of wavelengths

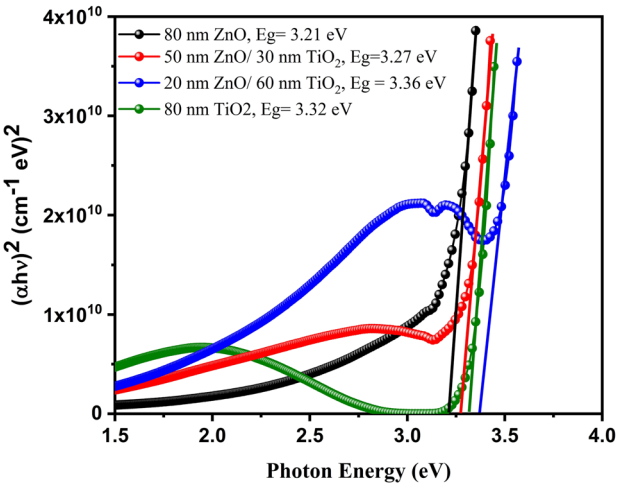

Fig. 5 Optical band gap (E_g) of single-layer ZnO, single-layer TiO_2, and bilayer ZnO/TiO_2 thin films, determined from the Tauc's equation

2000 nm for single layers of both ZnO and TiO_2, as well as for the ZnO/TiO_2 bilayer. All samples have an overall thickness of approximately 80 nm. It can be observed that the absorption coefficient increases as the thickness of the TiO_2 layer increases. The absorption coefficient was determined using Lambert's law, expressed by the following equation [67]:

$$\alpha = \frac{1}{t} \ln \frac{1}{T}, \tag{2}$$

where α is the absorption coefficient, t is the thin-film thickness, and T is the transmittance spectrum of thin film.

All samples exhibit sharp absorption edges in the 350–400 nm range. Furthermore, as seen in Fig. 4, the absorption edge shifts toward longer wavelengths as the thickness of the top ZnO layer increases. This shift is attributed to a change in the band gap of the bilayer samples. The bilayer samples also show a reduction in the wavelength range associated with a decrease in the absorption coefficient before reaching the sharp absorption edge. This behavior may be linked to an increase in defects at the interface between the two layers [68]. In addition, all synthesized bilayer ZnO/TiO_2 thin films exhibit significantly stronger and broader UV–visible absorption compared to the single-layer films, consistent with the findings reported by Lingxing Shi et al. [69]. The optical band-gap energy (E_g) of the samples was determined under the assumption that they behave as direct band-gap semiconductors, as shown in Fig. 5. Tauc's equation, $(\alpha h\nu)^2 = \beta(h\nu - E_g)$ [70], was used to analyze the absorption data. This involved plotting $(\alpha h\nu)^2$ on the y-axis against the incident photon energy $(h\nu)$ on the x-axis. The band-gap value was determined by extrapolating the linear portion of the plot to the x-axis [71]. The results of the E_g calculations are summarized in Table 1. The band-gap energy values for the single-layer ZnO and the single-layer TiO_2 are 3.21 eV and 3.32 eV, respectively. Numerous previous studies have investigated the energy band gap for ZnO and TiO_2. For instance, El-Hossary et al. [7] demonstrated that the energy band gap of ZnO varies between 3.14 and 3.35 eV, depending on changes in film thickness and surface morphology. Similarly, El-Moula et al. [72] reported that the E_g for TiO_2 ranges from 3.12 to 3.49 eV, influenced by the thickness of the Cu metal layer between the top and bottom TiO_2 thin films. Other studies have shown that the band gap of ZnO is approximately 3.2–3.37 eV, depending on the crystal quality of the films [73]. For bilayer films, the results indicate an increase in the energy band gap from 3.27 eV to 3.36 eV as the thickness of TiO_2 increases. This change in the energy band gap may be attributed to the structural transition from the semi-crystalline structure of ZnO to the amorphous structure of TiO_2 [74]. In addition, the interaction between the two layers, ZnO and TiO_2, promotes interfacial carrier transfer due to their matching band edge configurations. This transfer increases the concentration of carriers in both the

conduction and valence bands, which influences the electronic structure and subsequently alters the energy band-gap value. Moreover, the average grain size of composite samples plays a crucial role in determining their electronic properties by influencing charge transport, interfacial effects, defect density, and polarization mechanisms [75]. The grain size can significantly impact the band gap, particularly in semiconductor materials and composites. Smaller grain sizes typically lead to an increase in the band gap due to quantum size effects and the higher surface-to-volume ratio, which results in more localized electronic states [76, 77]. Therefore, optimizing grain size is essential for tailoring the electronic, dielectric, and functional properties of materials for specific applications. Abdel-Galil et al. [78] reported a slight increase in the optical band gap of ZnO from 3.2 eV to 3.218 eV. They attributed this rise in E_g to the combined effects of increased surface roughness and decreased crystallinity, which led to a higher density of defects. Research has shown that both oxygen excess and deficiency significantly influence electrical parameters, such as resistivity and both dc- and ac-band gaps. Trukhanov et al. demonstrated that oxygen deficiency in $La_{0.7}Ba_{0.3}MnO_{3-\gamma}$ ($0 \le \gamma \le 0.30$) can modify its magnetic and electrical behavior, a phenomenon also relevant to ZnO/TiO_2 bilayer [79]. These findings are in good agreement with the results obtained in the present study.

3.4 Photoluminescence properties

The PL spectra at RT for single-layer ZnO, single-layer TiO_2, and bilayer ZnO/TiO_2 thin films are shown in Fig. 6. All films exhibit PL emission peaks within the 400–550 nm range. Notably, the spectra display a strong violet emission at 420 nm, along with weaker emissions at 461 nm and 467 nm. Both single-layer ZnO and bilayer 50 nm ZnO/30 nm TiO_2 thin films show a strong violet emission at 420 nm and a green emission at 544 nm. The PL spectra of pure ZnO and 50 nm ZnO/30 nm TiO_2 thin films consist of a violet emission band and a broad visible emission band. Typically, UV emission is associated with the recombination of excited electrons and is influenced by the wavelength of the excitation light [80]. In contrast, visible luminescence is primarily attributed to structural defects, including zinc vacancies, oxygen vacancies, interstitial zinc, and interstitial oxygen, which are linked to deep-level emissions [81]. Interestingly, the violet emission at

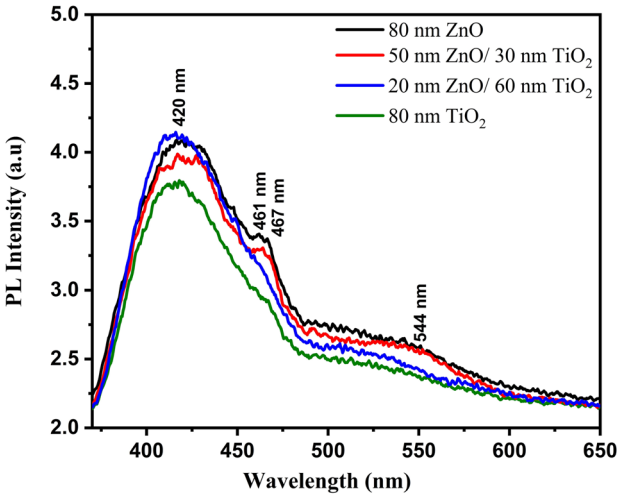

Fig. 6 Photoluminescence spectra of single-layer ZnO, single-layer TiO_2, and bilayer ZnO/TiO_2 thin films, showing the emission characteristics at RT

420 nm is significantly more intense than the green emission at 544 nm. In addition, the PL spectra of single-layer TiO_2 and 20 nm ZnO/60 nm TiO_2 thin films were measured under identical excitation intensity, and violet luminescence at approximately 420 nm was still observed. This leads to the conclusion that the violet emission is not solely due to amorphous or crystalline TiO_2 films. Several explanations have been proposed for violet emission. For example, violet luminescence at 420 nm has been attributed to an electron–hole plasma state under high excitation [82], while emission at 414 nm is associated with shallow defects under weak excitation intensity [83]. Cao et al. [84] suggested that violet emission arises from exciton recombination between electrons localized at shallow zinc donor levels and holes in the valence band. However, in their experiments, the violet luminescence band was not prominent at RT. In contrast, Lingxing Shi et al. [69] proposed that violet luminescence may originate from radiative defects associated with interface traps at grain boundaries, resulting from radiative transitions between these defect levels and the valence band. Furthermore, the appearance of green emission in the bilayer 50 nm ZnO/30 nm TiO_2 film is attributed to a reduction in the crystalline structure (amorphous nature) and a decrease in Zn content. Intrinsic defects, particularly oxygen vacancies and oxygen interstitials, are significant contributors to the green and yellow regions of the PL spectra in

ZnO [85]. Zhou et al. [86] suggested that the possible presence of $Zn(OH)_2$ on the surface could also contribute to the green emission. In addition, the enhanced UV emission observed in the 20 nm ZnO/60 nm TiO_2 sample can be explained by two factors: (1) the surface passivation effect caused by capping TiO_2 particles, and (2) fluorescence resonance energy transfer (FRET) between the band edge transitions of TiO_2 and ZnO [87]. FRET involves the non-radiative transfer of photon energy from an excited donor to an acceptor located in close proximity. For FRET to occur, the absorption spectrum of the acceptor must overlap with the fluorescence spectrum of the donor, and the transition dipole orientations of the donor and acceptor must have a parallel component [87]. The transmittance spectra of the films revealed that the band gaps of TiO_2 and ZnO are comparable, and their luminescence spectra overlap significantly, suggesting the possibility of FRET. When the ZnO/TiO_2 bilayer films are irradiated with UV light, photo-induced electrons (e^-) can transfer from the conduction band (CB) of TiO_2 to that of ZnO [88]. Simultaneously, holes (h^+) migrate from the valence band (VB) of TiO_2 to that of ZnO. This charge carrier accumulation broadens the band gap of the bilayer films, which aligns with the transmittance results. Furthermore, this process increases the probability of electron–hole recombination luminescence. Specifically, energy is efficiently transferred to ZnO after the excitation of electron–hole pairs in TiO_2 via the resonance effect, leading to a significant enhancement of the band edge emission of ZnO. As a result, the UV emission intensity increases with the thickness of the TiO_2 layer, peaking at the 20 nm ZnO/60 nm TiO_2 film. In conclusion, the structural transition from crystalline to amorphous reduces the intensity of PL emission and decreases the electron–hole recombination rate. This structural change in the bilayer samples promotes enhanced electron–hole separation, significantly improving their photocatalytic activity [89, 90].

4 Conclusion

This study investigated the structural, morphological, and optical properties of ZnO/TiO_2 bilayer thin films deposited via pulsed DC magnetron sputtering. The bilayer films exhibited approximately double the surface roughness compared to single-layer films, while the adhesion force decreased with increasing TiO_2 thickness, from 50 mN (80 nm ZnO) to 10 mN (80 nm TiO_2). XRD analysis revealed a semi-crystalline hexagonal wurtzite structure for ZnO and an amorphous phase for TiO_2. Optical characterization showed a redshift in the absorption edge as the ZnO thickness increased and a rise in the optical band gap with thicker TiO_2, which can be attributed to structural changes and interfacial interactions. Photoluminescence spectroscopy revealed a strong violet emission at 420 nm, with UV emission intensity peaking for the 20 nm ZnO/60 nm TiO_2 configuration. These findings highlight the enhanced optical properties of ZnO/TiO_2 bilayer thin films, suggesting their potential for optoelectronic applications.

Future research will focus on optimizing the properties of ZnO/TiO_2 bilayer films for specific optoelectronic applications. In particular, the effects of varying deposition parameters, such as sputtering power, pressure, and substrate temperature, on film morphology, crystallinity, and optical properties will be further explored. In addition, the role of interfacial interactions between ZnO and TiO_2 will be studied in greater detail, with an emphasis on their impact on charge transport and recombination dynamics.

Author contributions

All authors have made significant contributions to this research paper. MHF: conceived and designed the study, developed the methodology, supervised the research, and provided critical revisions to the manuscript. AAAE-M: contributed to the study design, conducted the literature review, interpreted the data, and drafted sections of the manuscript. FME-H: provided technical expertise, revised the manuscript, and ensured the integrity of the research. TH: assisted with the methodology and data collection. MAE-K: conducted data analysis, drafted sections of the manuscript, assisted with manuscript preparation, and contributed to the validation processes. All authors reviewed and approved the final version of the manuscript.

Funding

Open access funding provided by The Science, Technology & Innovation Funding Authority (STDF) in

cooperation with The Egyptian Knowledge Bank (EKB). The authors report that this research was financial support provided by the Science, Technology & Innovation Funding Authority (STDF) under grant number 46027. This funding was instrumental in facilitating the research and its outcomes.

Data availability

Not Applicable.

Code availability

Not Applicable.

Declarations

Conflict of interest The authors declare that there are no conflicts of interest regarding the publication of this paper. No financial, personal, or professional relationships influenced the research or its outcomes.

Ethical approval This article does not involve any studies or experiments conducted on human participants or animals by any of the authors.

References

1. E.R. Rwenyagila, B. Agyei-Tuffour, M.G. Zebaze Kana, O. Akin-Ojo, W.O. Soboyejo, J. Mater. Res. **29**, 2912 (2014)
2. K. Sivaramakrishnan, T.L. Alford, Appl. Phys. Lett. (2010). https://doi.org/10.1063/1.3435467
3. D.C. Look, Mater. Sci. Eng. B **80**, 383 (2001)
4. T. Minami, Semicond. Sci. Technol. **20**, S35 (2005)
5. A. Wibowo, M.A. Marsudi, M.I. Amal, M.B. Ananda, R. Stephanie, H. Ardy, L.J. Diguna, RSC Adv. **10**, 42838 (2020)
6. Y. Kumari, L.K. Jangir, A. Kumar, *Nanostructured Zinc Oxide* (Elsevier, Amsterdam, 2021)
7. F.M. El-Hossary, S.H. Mohamed, E.A. Noureldein, M. Abo EL-Kassem, Mater. Sci. Semicond. Process. **120**, 105284 (2020)
8. F.M. El-Hossary, A. Ghitas, A.M.A. El-Rahman, A.A. Ebnalwaled, M.A. Shahat, M.H. Fawey, J. Mater. Sci. Mater. Electron. **32**, 15718 (2021)
9. Y. Zhang, X. Xu, Optik (Stuttg). **217**, 164808 (2020)
10. S. Ge, D. Sang, L. Zou, Y. Yao, C. Zhou, H. Fu, H. Xi, J. Fan, L. Meng, C. Wang, Nanomaterials **13**, 1141 (2023)
11. L.E. Pérez-Jiménez, J.C. Solis-Cortazar, L. Rojas-Blanco, G. Perez-Hernandez, O.S. Martinez, R.C. Palomera, F. Paraguay-Delgado, I. Zamudio-Torres, E.R. Morales, Res. Phys. **12**, 1680 (2019)
12. E. Mosquera-Vargas, D. Herrera-Molina, J.E. Diosa, Rev. UIS Ing. (2022). https://doi.org/10.18273/revuin.v21n3-2022007
13. Y. Zhang, X. Xu, Phys. C Supercond. Appl. **592**, 1353998 (2022)
14. Y. Zhang, X. Xu, Appl. Phys. A **126**, 341 (2020)
15. D.A. Vinnik, A.Y. Starikov, V.E. Zhivulin, K.A. Astapovich, V.A. Turchenko, T.I. Zubar, S.V. Trukhanov, J. Kohout, T. Kmječ, O. Yakovenko, L. Matzui, A.S.B. Sombra, D. Zhou, R.B. Jotania, C. Singh, A.V. Trukhanov, Ceram. Int. **47**, 17293 (2021)
16. V.A. Turchenko, S.V. Trukhanov, A.M. Balagurov, V.G. Kostishyn, A.V. Trukhanov, L.V. Panina, E.L. Trukhanova, J. Magn. Magn. Mater. **464**, 139 (2018)
17. H. Albetran, H. Haroosh, Y. Dong, V.M. Prida, B.H. O'Connor, I.M. Low, Appl. Phys. A **116**, 161 (2014)
18. D.A.H. Hanaor, C.C. Sorrell, J. Mater. Sci. **46**, 855 (2011)
19. Y. Zhang, J. Li, S. Che, Y. Tian, Met. Mater. Int. **26**, 783 (2020)
20. Y. Zhang, X. Xu, ACS Omega **5**, 15344 (2020)
21. Y. Ku, Y.-H. Huang, Y.-C. Chou, J. Mol. Catal. A Chem. **342–343**, 18 (2011)
22. L. Wang, X. Fu, Y. Han, E. Chang, H. Wu, H. Wang, K. Li, X. Qi, J. Nanomater. **2013**(1), 321459 (2013)

23. T. Giannakopoulou, N. Todorova, M. Giannouri, J. Yu, C. Trapalis, Catal. Today **230**, 174 (2014)
24. M.A. Almessiere, Y. Slimani, N.A. Algarou, M.G. Vakhitov, D.S. Klygach, A. Baykal, T.I. Zubar, S.V. Trukhanov, A.V. Trukhanov, H. Attia, M. Sertkol, İA. Auwal, Adv. Electron. Mater. **8**, 2101124 (2022)
25. Y. Guo, D. Zhou, D. Li, W. Zhao, Y. Wang, L. Pang, Z. Shi, T. Zhou, S. Sun, C. Singh, S. Trukhanov, A.S.B. Sombra, G. Chen, J. Mater. Chem. C **11**, 6999 (2023)
26. T.D. Malevu, Phys. B Condens. Matter **621**, 413291 (2021)
27. J. Li, J. Li, N. Ma, L. Guan, C. Tan, Z. Xia, J. Xu, J. Zuo, Chem. Phys. Lett. **838**, 141084 (2024)
28. H.H. Lemago, L. Tolezani, T. Igricz, D. Hessz, P. Pál, C. Cserháti, G. Vecsei, B. Sárközi, E.M. Baradács, Z. Erdélyi, I.M. Szilágyi, Ceram. Int. **51**, 339 (2025)
29. Y.S.M. Elzawiei, M.R. Hashim, A. Abdulhameed, M.M. Halim, Phys. B Condens. Matter **697**, 416734 (2025)
30. H.D.O. Barros, R.F. Abreu, T.O. Abreu, W.V. Sousa, F.E. Nogueira, F.F. Carmo, J.E. Morais, J.P. Nascimento, M.A. Silva, R.S. Silva, S.V. Trukhanov, Phys. B: Condens. Matter **695**, 416547 (2024)
31. I.V. Bodnar, V.V. Khoroshko, V.A. Yashchuk, V.F. Gremenok, M. Kazi, M.U. Khandaker, T.I. Zubar, D.I. Tishkevich, A.V. Trukhanov, S.V. Trukhanov, J. Cryst. Growth **626**, 127481 (2024)
32. D.R. Sahu, J.-L. Huang, Mater. Sci. Eng. B **130**, 295 (2006)
33. R. Hussin, K.L. Choy, X.H. Hou, Appl. Mech. Mater. **465–466**, 916 (2013)
34. K.-S. Kim, H.W. Kim, C.M. Lee, Mater. Sci. Eng. B **98**, 135 (2003)
35. J.-L. Chung, J.-C. Chen, C.-J. Tseng, Appl. Surf. Sci. **255**, 2494 (2008)
36. I. Saurdi, M.H. Mamat, M. Rusop, Adv. Mater. Res. **667**, 206 (2013)
37. N.C. Raut, T. Mathews, P. Chandramohan, M.P. Srinivasan, S. Dash, A.K. Tyagi, Mater. Res. Bull. **46**, 2057 (2011)
38. N. Naseri, P. Sangpour, A.Z. Moshfegh, Electrochim. Acta **56**, 1150 (2011)
39. I.O. Troyanchuk, D.D. Khalyavin, S.V. Trukhanov, G.N. Chobot, H. Szymczak, J. Exp. Theor. Phys. Lett. **70**, 590 (1999)
40. A.I. Stognij, N.N. Novitskii, S.V. Trukhanov, A.V. Trukhanov, L.V. Panina, S.A. Sharko, A.I. Serokurova, N.N. Poddubnaya, V.A. Ketsko, V.P. Dyakonov, H. Szymczak, C. Singh, Y. Yang, J. Magn. Magn. Mater. **485**, 291 (2019)
41. S. Sabet, A. Moradabadi, S. Gorji, M. Yi, Q. Gong, M.H. Fawey, E. Hildebrandt, D. Wang, H. Zhang, B.-X. Xu, C. Kübel, L. Alff, Phys. Rev. B **98**, 174440 (2018)
42. S. Sabet, A. Moradabadi, S. Gorji, M.H. Fawey, E. Hildebrandt, I. Radulov, D. Wang, H. Zhang, C. Kübel, L. Alff, Phys. Rev. Appl. **11**, 054078 (2019)
43. M. Garbrecht, L. Hultman, M.H. Fawey, T.D. Sands, B. Saha, Phys. Rev. Mater. **1**, 033402 (2017)
44. M.R. Chellali, S.H. Nandam, S. Li, M.H. Fawey, E. Moreno-Pineda, L. Velasco, T. Boll, L. Pastewka, R. Kruk, P. Gumbsch, H. Hahn, Acta Mater. **161**, 47 (2018)
45. F.M. El-Hossary, N.Z. Negm, A.M.A. El-Rahman, M. Hammad, C. Templier, Surf. Coat. Technol. **202**, 1392 (2008)
46. M. Garbrecht, L. Hultman, M.H. Fawey, T.D. Sands, B. Saha, J. Mater. Sci. **53**, 4001 (2018)
47. G.V. Ashok Reddy, K. Naveen Kumar, S.A. Sattar, H.D. Shetty, N.G. Prakash, R. Imran Jafri, C. Devaraja, B.C. Manjunatha, C.S. Kaliprasad, R. Premkumar, S. Ansar, Phys. B Condens. Matter. **664**, 414996 (2023)
48. P. Devaraj, P. Peranantham, Y.L. Jeyachandran, Phys. B Condens. Matter. **691**, 416315 (2024)
49. Z. Li, B. Mi, X. Ma, P. Liu, F. Ma, K. Zhang, X. Chen, X. Zhu, Y. Meng, H. Lu, W. Li, Vacuum **228**, 113518 (2024)
50. G. Wisz, P. Sawicka-Chudy, A. Wal, P. Potera, M. Bester, D. Płoch, M. Sibiński, M. Cholewa, M. Ruszała, Appl. Mater. Today **29**, 101673 (2022)
51. M. Pérez-González, S.A. Tomás, J. Santoyo-Salazar, M. Morales-Luna, Ceram. Int. **43**, 8831 (2017)
52. Y.-H. Wang, K.H. Rahman, C.-C. Wu, K.-C. Chen, Catalysts **10**, 598 (2020)
53. B. Abdallah, A.K. Jazmati, R. Refaai, Mater. Res. **20**, 607 (2017)
54. G. Yergaliuly, B. Soltabayev, S. Kalybekkyzy, Z. Bakenov, A. Mentbayeva, Sci. Rep. **12**, 851 (2022)
55. N. Nosidlak, J. Jaglarz, A. Vallati, P. Dulian, M. Jurzecka-Szymacha, S. Gierałtowska, A. Seweryn, Ł Wachnicki, B.S. Witkowski, M. Godlewski, Coatings **13**, 1872 (2023)
56. C.M. Firdaus, M.S.B.S. Rizam, M. Rusop, S.R. Hidayah, Procedia Eng. **41**, 1367 (2012)
57. I. Saurdi, A. K. Shafura, N. E. A. Azhar, A. Ishak, M. F. Malek, A. H. S. Alrokayan, H. A. Khan, M. H. Mamat, and M. Rusop, in (2016), p. 020063.
58. F.M. El-Hossary, A.M.A. El-Rahman, M. Raaif, S. Qu, J. Zhao, M.F. Maitz, M.A. ELKassem, Appl. Phys. A **124**, 42 (2018)
59. Y. Zhuang, Q. Huang, W. Tan, R. Qi, H. Zhou, Z. Zhang, Z. Wang, Appl. Opt. **61**, 5769 (2022)
60. P. Heidari, M. Salehi, B. Ruhani, V. Purcar, S. Căprărescu, Materials (Basel). **15**, 2102 (2022)
61. P. Scherrer, Nachrichten von Der Gesellschaft Der Wissenschaften Zu Göttingen. Math. Klasse **1918**, 98 (1918)

62. Y. Sagidolda, S. Yergaliyeva, Z. Tolepov, G. Ismailova, B. Orynbay, R. Nemkayeva, O. Prikhodko, S. Peshaya, S. Maksimova, N. Guseinov, Y. Mukhametkarimov, Materials (Basel). **16**, 6809 (2023)
63. M. Aykol, A. Merchant, S. Batzner, J. N. Wei, and E. D. Cubuk, Nat. Comput. Sci. (2024).
64. L. Xu, X. Li, Y. Chen, F. Xu, Appl. Surf. Sci. **257**, 4031 (2011)
65. E. Bacaksiz, S. Aksu, S. Yılmaz, M. Parlak, M. Altunbaş, Thin Solid Films **518**, 4076 (2010)
66. Y. Chen, C. Zhang, W. Huang, C. Yang, T. Huang, Y. Situ, H. Huang, Surf. Coat. Technol. **258**, 531 (2014)
67. M.H. Mamat, M.Z. Sahdan, Z. Khusaimi, A.Z. Ahmed, S. Abdullah, M. Rusop, Opt. Mater. (Amst). **32**, 696 (2010)
68. W.A.C.P. Wanniarachchi, T. Arunasalam, P. Ravirajan, D. Velauthapillai, P. Vajeeston, ACS Omega **8**, 42275 (2023)
69. L. Shi, H. Shen, L. Jiang, X. Li, Mater. Lett. **61**, 4735 (2007)
70. R. Ziegler, Monatskurse Fur Die Arztl. Fortbildung **31**, 63 (1981)
71. M.A. Butler, J. Appl. Phys. **48**, 1914 (1977)
72. A.A.A. El-Moula, F.M. El-Hossary, M. Raaif, A. Thabet, M.A. El-Kassem, J. Electron. Mater. **50**, 2699 (2021)
73. P. Lv, W. Zheng, L. Lin, F. Peng, Z. Huang, F. Lai, Phys. B Condens. Matter **406**, 1253 (2011)
74. B.I. Stefanov, Coatings **13**, 1568 (2023)
75. S.V. Trukhanov, L.S. Lobanovski, M.V. Bushinsky, V.V. Fedotova, I.O. Troyanchuk, A.V. Trukhanov, V.A. Ryzhov, H. Szymczak, R. Szymczak, M. Baran, J. Phys. Condens. Matter **17**, 6495 (2005)
76. M.T. Ahmed, S. Islam, F. Ahmed, Adv. Condens. Matter Phys. **2022**, 1 (2022)
77. H.V. Ganvir, Commun. Appl Nonlinear Anal. **32**, 113 (2024)
78. A. Abdel-Galil, M.S.A. Hussien, M.R. Balboul, J. Aust. Ceram. Soc. **58**, 1667 (2022)
79. S.V. Trukhanov, I.O. Troyanchuk, N.V. Pushkarev, H. Szymczak, J. Exp. Theor. Phys. **95**, 308 (2002)
80. C.-C. Lin, H.-P. Chen, H.-C. Liao, S.-Y. Chen, Appl. Phys. Lett. **86**, 183103 (2005)
81. Y.G. Wang, S.P. Lau, H.W. Lee, S.F. Yu, B.K. Tay, X.H. Zhang, H.H. Hng, J. Appl. Phys. **94**, 354 (2003)
82. G. Tobin, E. McGlynn, M.O. Henry, J.-P. Mosnier, E. de Posada, J.G. Lunney, Appl. Phys. Lett. (2006). https://doi.org/10.1063/1.2174107
83. X.-P. Shen, A.-H. Yuan, Y.-M. Hu, Y. Jiang, Z. Xu, Z. Hu, Nanotechnology **16**, 2039 (2005)
84. B. Cao, W. Cai, H. Zeng, Appl. Phys. Lett. (2006). https://doi.org/10.1063/1.2195694
85. D. Li, Y.H. Leung, A.B. Djurišić, Z.T. Liu, M.H. Xie, S.L. Shi, S.J. Xu, W.K. Chan, Appl. Phys. Lett. **85**, 1601 (2004)
86. H. Zhou, H. Alves, D.M. Hofmann, W. Kriegseis, B.K. Meyer, G. Kaczmarczyk, A. Hoffmann, Appl. Phys. Lett. **80**, 210 (2002)
87. H.Y. Lin, Y.Y. Chou, C.L. Cheng, Y.F. Chen, Opt. Exp. **15**, 13832 (2007)
88. X. Jiang, X. Zhao, L. Duan, H. Shen, H. Liu, T. Hou, F. Wang, Ceram. Int. **42**, 15160 (2016)
89. R.A. Shathy, S.A. Fahim, M. Sarker, M.S. Quddus, M. Moniruzzaman, S.M. Masum, M.A.I. Molla, Catalysts **12**, 308 (2022)
90. Q. Zhang, C. Li, Nanomaterials **9**, 1339 (2019)